In vivo characterization of activatable cell penetrating peptides for targeting protease activity in cancer†

Emilia S. Olson,‡[ae] Todd A. Aguilera,‡[ae] Tao Jiang,[af] Lesley G. Ellies,[b] Quyen T. Nguyen,[c] Edmund H. Wong,[d] Larry A. Gross[af] and Roger Y. Tsien*[af]

Activatable cell penetrating peptides (ACPPs) are novel *in vivo* targeting agents comprised of a polycationic cell penetrating peptide (CPP) connected *via* a cleavable linker to a neutralizing polyanion (Fig. 1A). Adsorption and uptake into cells are inhibited until the linker is proteolyzed. An ACPP cleavable by matrix metalloproteinase-2 (MMP-2) *in vitro* was the first one demonstrated to work in a tumor model *in vivo*, but only HT-1080 xenografts and resected human squamous cell carcinomas were tested. Generality to other cancer types, *in vivo* selectivity of ACPPs for MMPs, and spatial resolution require further characterization. We now show that ACPPs can target many xenograft tumor models from different cancer sites, as well as a thoroughly studied transgenic model of spontaneous breast cancer (mouse mammary tumor virus promoter driving polyoma middle T antigen, MMTV-PyMT). Pharmacological inhibitors and genetic knockouts indicate that current ACPPs are selective for MMP-2 and MMP-9 in the above *in vivo* models. In accord with the known local distribution of MMP activity, accumulation is strongest at the tumor–stromal interface in primary tumors and associated metastases, indicating better spatial resolution (< 50 μm) than other currently available MMP-cleavable probes. We also find that background uptake of ACPPs into normal tissues such as cartilage can be decreased by appending inert macromolecules of 30–50 KDa to the polyanionic inhibitory domain. Our results validate an approach that should generally deliver imaging agents and chemotherapeutics to sites of invasion, tumor-promoting inflammation, and metastasis.

Introduction

In most types of solid tumors, the gelatinases MMP-2 and MMP-9 are upregulated, and play complex roles the promotion of tumorigenesis by degrading the extracellular matrix, activating growth factors, and activating angiogenesis.[1–5] Probes that non-invasively detect the activity of these proteases *in vivo* would be of great interest to help understand basic tumor biology, monitor the development and growth of tumors, and assay the effectiveness of MMP inhibitors. Previous probes have been based on active site inhibitors,[6,7] fluorescence dequenching,[8–10] removal of solubilizing groups[11] and ACPPs,[12–14] but the spatial resolution, biodistribution and generality of tumor targeting of all these approaches require much further characterization. Here, we have tested the ability of ACPPs to image MMP activity in a wide variety of tumor models representing different cancer types. Unlike many other targeted contrast agents such as antibodies, the basic unit of the ACPP is only 3.5 kDa, which should allow

[a] *Department of Pharmacology, La Jolla, CA 92093-0647, USA*
[b] *Department of Pathology, La Jolla, CA 92093-0647, USA*
[c] *Department of Surgery, La Jolla, CA 92093-0647, USA*
[d] *Department of Radiology, La Jolla, CA 92093-0647, USA*
[e] *Medical Scientist Training Program, La Jolla, CA 92093-0606, USA*
[f] *Howard Hughes Medical Institute and University of California at San Diego, La Jolla, CA 92093-0647, USA. E-mail: rtsien@ucsd.edu*
† Electronic supplementary information (ESI) available: Methods, additional figures and LC mass spectra. See DOI: 10.1039/b904890a
‡ These authors contributed equally.

Insight, innovation, integration

Our companion paper discusses advantages of activatable cell penetrating peptides (ACPP) compared to parent cell penetrating peptides (CPP). Here we describe the validation of ACPPs for targeting disease-associated proteases (matrix metalloproteases) in cancer and cancer metastases. Additionally, we propose our solution to the problems of rapid pharmacokinetics and high background of ACPPs by adding macromolecular carriers to modulate pharmacokinetic distribution in animals. We show that this technology can be used to target enzymes associated with cancer, which could have broad applicability to other pathologies where extracellular enzymes play important roles. This paper demonstrates how rational design and validation of exogenous probes could enable scientists to ask previously difficult questions and provide a platform for the development of imaging and therapeutic agents.

better penetration into solid tumors. Also, each active enzyme molecule can cleave many substrate ACPPs, offering amplification instead of mere stoichiometric binding. To examine the usefulness of ACPPs for future design of contrast agents and drug delivery vehicles, here we have addressed some basic questions regarding specificity of linker cleavage and ACPP uptake *in vitro* and *in vivo*, as well as the spatial resolution of probe accumulation.

Results

Pharmacological inhibitors of MMP-2 and MMP-9 activity reduce selective ACPP uptake by tumor xenografts

Immunodeficient mice harboring HT-1080 human fibrosarcoma xenografts were injected intravenously with either the MMP-cleavable ACPP Suc-e_8-xPLGLAG-r_9-c(Cy5), its all-D-amino acid, cleavage resistant negative control, Suc-e_8-xplglag-r_9-k(Cy5), or a "universal negative control", Suc-e_8-(PEG2)$_2$-r_9-c(Cy5). Suc denotes succinyl, lowercase letters represent D-amino acids, x is 6-aminohexanoyl, PEG2 is $-NH(CH_2CH_2O)_2CH_2CO-$, and Cy5 is a deep-red fluorescent label. The advantages of the all-D-amino acid

control are that it exactly matches the hydrophobicity and molecular weight of the cleavable ACPP, yet it cannot be cleaved by purified enzymes such as MMP-2 and MMP-9. However, absolute resistance to all proteases cannot be guaranteed, especially because of the two achiral glycine residues. The advantage of the PEG2-linked control is that we have never seen significant cleavage in any tissue, though its hydrophobicity and molecular weight do not exactly match cleavable ACPP. Fig. 1A shows two images of representative mice after sacrifice and skin removal six hours post injection to show the visual contrast between the cleavable peptide and D-amino acid control in the tumors (arrows). Serial images were taken for six hours after injection. Fluorescence intensity was measured for regions over the tumor ("tumor") and the thorax ("background"), generating curves of the form shown in Fig. 1B. Though the "tumor-to-background ratio" is a standard method for evaluating molecular imaging probes, we found it could vary significantly by choosing different regions on the animal to serve as "background", likely due to tissue geometry (ESI, Fig. S1†). To generate more quantitative data at one time point, the animals were sacrificed at six hours and the organs were harvested. Standardized
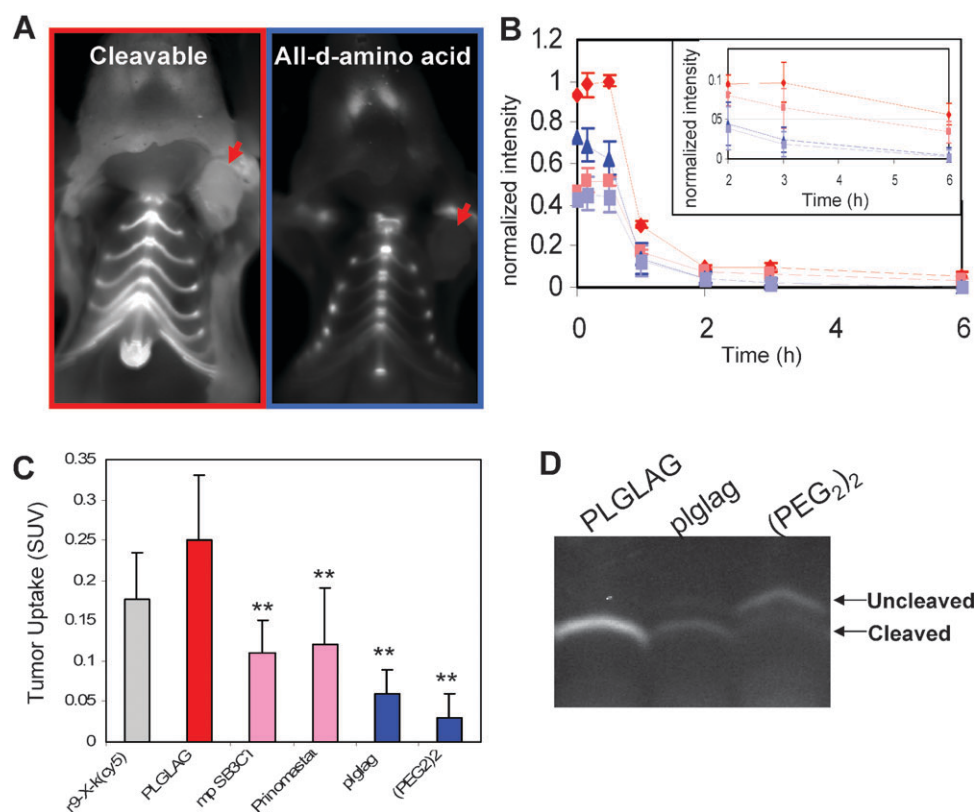

Fig. 1 Uptake of free ACPPs by mice harboring HT-1080 xenografts is protease dependent. (A) Images of nude mice bearing HT-1080 xenografts six hours after injection with either cleavable ACPP or an all-D-amino acid control. The skin has been removed to expose the tumor (red arrows). (B) Shows a washout curve generated from taking regions over the tumor (red or blue) and thorax (pink or light blue, dashed lines) of animals receiving 10 nmol of either cleavable suc-e_8-xPLGLAG-r_9-c(Cy5) (n = 3) (red diamonds or pink squares) or suc-e_8-xplglag-r_9-k(Cy5) (n = 3) (blue triangles or light blue squares), respectively. Error bars represent standard deviations. (C) Tumor uptake of peptide in animals decreased when pre-injected with pharmacological inhibitors of MMPs (SB3CT or prinomastat). Uptake values for the r_9-x-k(cy5) CPP probe as well as the all-D-amino acid and 2 unit PEG linker control peptides are shown for reference. r_9-x-k(Cy5) n = 3, PLGLAG n = 9, SB3CT n = 3, Prinomastat n = 3, plglag n = 8, (PEG2)$_2$ n = 3. Error bars represent standard deviation. ** represents statistically significant difference from the cleavable ACPP using a two tailed t-test. (D) Polyacrylamide gel electrophoresis of tumor homogenates differentiates cleaved vs. intact peptides recovered from tumors of IV injected mice.

uptake values (molality in tissue/molality injected into mouse, abbreviated as SUV) were measured by homogenizing a fixed amount of tissue in an SDS-containing buffer and comparing the resultant fluorescence intensity with a calibration curve made by spiking matching tissue homogenates from uninjected animals with varying amounts of peptide (Fig. 1C and ESI, Fig. S2†). This analysis, which theoretically eliminated variability from tissue geometry and quenching, demonstrated a 4.1-fold difference in fluorescence for tumors from animals injected with cleavable peptide when compared to those injected with the D-amino acid version of the same peptide as the negative control ($p < 0.0005$). The SUV value for tumors from animals injected with the control ACPP with a $(PEG2)_2$ linker was half that of tumors from animals injected with the D-amino acid control, yielding an 8-fold contrast with cleavable peptide (Table 1), again suggesting potential cleavage of the D-amino acid control by HT-1080 xenografted tumors. Nearly complete cleavage of the cleavable peptide in HT-1080 tumors was confirmed by gel electrophoresis and mass spectrometry, yielding $G-r_9-c(Cy5)$ and $r_9-c(Cy5)$ (Fig. 1D and ESI, Fig. S3†). Gel electrophoresis confirmed that the ACPP was indeed fully cleaved in the tumor, whereas the D-amino acid control peptide was partially cleaved and the $(PEG2)_2$ control peptide remained almost completely intact (Fig. 1D). It should be noted that the extent of cleavage is somewhat exaggerated by this assay, because uncleaved peptides are much less well retained within the tumor. Although we have not recovered enough material for mass spectrometry to determine the fate of the D-amino acid control peptide within the tumor, this peptide yields $lag-r_9-c(Cy5)$ in the liver and kidney, implying cleavage after the first glycine.

To determine whether uptake of the ACPP peptide in xenografts required MMP activity, we pre-injected the broad-spectrum MMP family inhibitor prinomastat[15] and the more gelatinase-specific inhibitor membrane permeable SB-3CT.[16] This resulted in 65%–75% inhibition for HT-1080s ($n = 3$ for SB-3CT, $n = 3$ for prinomastat), suggesting that most of the peptide cleavage is due to MMP-2 and -9. SUV averages and standard deviations for HT-1080 tumors from animals injected in the presence and absence of inhibitors are shown in Fig. 1C and Table 1. The lack of complete inhibition could reflect either pharmacokinetic clearance of inhibitor following a single dose, or the ability of other enzymes to cut the linker.

Uptake of ACPPs occurs in a wide variety of tumor types in immunodeficient and immunocompetent animals

An advantage of MMPs as targets for ACPPs is that inflammation and associated MMP activation are involved in the

Table 1 Tumor standardized uptake values for ACPP's of the form $suc-e_8-x^{******}r_9-c(Cy5)$

	PLGLAG	plglag	p-value	Ratio	PLGLAG + inhibitor	p-value	% inhibition[a]
HT-1080 (fibrosarcoma)	0.25 ± 0.08 (0.14–0.41) $n = 9$	0.06 ± 0.03 (0–0.12) $n = 8$	3E-5	4.10	Prinomastat 0.12 ± 0.07 (0.06–0.19) $n = 3$ SB3CT 0.11 ± 0.04 (0.08–0.15) $n = 3$	0.05 0.003	66% 75%
B16F10 (melanoma)	0.24 ± 0.06 (0.17–0.32) $n = 4$	0.07 ± 0.02 (0.05–0.08) $n = 4$	0.009	3.77	—	—	—
Hep2 (cervical)	0.42 ± 0.14 (0.26–0.53) $n = 3$	0.09 ± 0.03 (0.07, 0.12) $n = 2$	0.048	4.67	SB3CT 0.13 (0.13) $n = 1$	—	88%
PC3 (prostate)	0.15 ± 0.05 (0.11–0.23) $n = 7$	0.03 $n = 1$	—	5.00	—	—	—
HCT (colon)	0.45 ± 0.16 (0.57, 0.33) $n = 2$	0.13 ± 0.06 (0.08, 0.17) $n = 2$	0.19	3.46	—	—	—
PyMT (mouse breast transgenic)	0.51 ± 0.05 (0.45–0.58) $n = 5$	0.14 ± 0.06 (0.07–0.23) $n = 5$	1E-6	3.64	$MMP2^{-/-}$ 0.39 ± 0.09 (0.30–0.46) $n = 3$ $MMP9^{-/-}$ 0.52 ± 0.10 (0.44–0.63) $n = 3$ $MMP9^{-/-}2^{+/-}$ 0.45 ± 0.03 (0.43, 0.47) $n = 2$ $MMP2^{-/-}9^{+/-}$ 0.21 ± 0.03 (0.18–0.24) $n = 3$ $MMP2^{-/-}9^{-/-}$ 0.18 ± 0.10 (0.08–0.28) $n = 3$	0.13 0.84 0.14 1E-4 0.02	31% −0.04% (no inhibition) 15% 81% 89%
Clone 8119 (derived from PyMT)	0.39 ± 0.12 (0.23–0.56) $n = 5$	0.17 ± 0.06 (0.12–0.23) $n = 4$	0.009	2.29	—	—	—
Clone 230 (derived from PyMT)	0.24 ± 0.27 (0.05, 0.43) $n = 2$	0.04 ± 0.05 (ND, 0.08) $n = 2$	0.48	6	—	—	—

[a] Percent inhibition = $(SUV_{cleavable} − SUV_{inhibitor})/(SUV_{cleavable} − SUV_{uncleavable})$

development and progression of many types of solid tumors.[2–5,17,18] We tested whether the uptake of ACPPs is a robust mechanism for targeting a wide variety of tumors derived from different tissue types. Some of these (B16 melanoma, mammary adenocarcinoma derived from PyMT transgenic model) were mouse-derived cell lines and could be injected into immunocompetent hosts. Other cell lines such as HCT-116 (colon), PC3 (prostate) and Hep2 (cervical[19]) were derived from human tumors, and needed to be injected into immunocompromised hosts. Standardized uptake values and p-values comparing tumors from animals injected with cleavable vs. uncleavable peptides are given in Table 1. Selective uptake, i.e. the ratio of tumor SUVs between L- and D-amino acid versions, varied between 2.3 and 6-fold depending on the model tested, with the variation probably being largely due to differences in the vascularity, level of necrosis (in larger tumors), and MMP activity of each tumor type. The level of MMP activity varied but baseline activity was verified by zymography in all excised tumors tested (ESI, Fig. S4†).

ACPPs are taken up selectively in regions of MMP activity in a transgenic tumor model

To determine whether MMP-cleavable ACPPs yield selective uptake in spontaneous tumors from immunocompetent animals, PyMT mice were injected with cleavable and cleavage-resistant ACPPs.[20] To confirm that there was MMP-dependent uptake of the ACPP-based peptides in this model, we injected the cleavable ACPP, the r_9-c(Cy5) CPP control (discussed in Aguilera et al.[21]) and both control peptides previously discussed intravenously, and imaged the animals after six hours with the skin removed. As expected, tumors from animals receiving the cleavable peptide were clearly brighter than tumors from animals receiving the

D-amino acid control peptide (Fig. 2A). For further confirmation of MMP-2 and MMP-9 dependent uptake, PyMT mice were bred with mice that lacked one or both genes for MMP-2 and/or MMP-9.[22] Zymography of tumors from PyMT mice with normal alleles for MMP-2 and MMP-9 showed activation of MMP-2, but little MMP-9 (ESI, Fig. S4 and S5†). Knocking out MMP-9 had little effect, neither on the uptake of peptide (Fig. 2B and Table 1) nor on the overall gelatinase activity. In contrast, knocking out MMP-2 had a variable phenotype with regard to peptide uptake, with the overall tumor uptake decreasing by only 31% ($n = 3$, $p = 0.13$). This result was also explained by gelatin zymography, which revealed that MMP-2 knockout mice often upregulate MMP-9, particularly if both alleles of the MMP-9 gene are present. If one allele of MMP-9 is knocked out in addition to both alleles of MMP-2, tumor uptake decreases by about 81% ($n = 3$). If both alleles of MMP-2 and MMP-9 are knocked out, the inhibition was 89% complete ($n = 3$), with the average tumor values not significantly different from those of the D-amino acid or (PEG2)$_2$ negative controls. The (PEG2)$_2$ control peptide varied significantly in animals with larger tumors vs. those with smaller tumors in the PyMT animals, as well as many of the xenografts with large, fast growing tumors (B16-F10); this is likely due to its uptake in areas of necrosis (ESI, Fig. S6†).

ACPP uptake occurred at the tumor–stroma interface where MMP activity was highest in PyMT tumors

In addition to the ability to breed genetic knockouts, the PyMT model has the major advantage that mammary tissue undergoes a predictable progression from ductal hyperplasia to mammary adenocarcinoma to frank carcinoma and lung metastasis.[20,23] Particularly in adenomatous tumors, there is
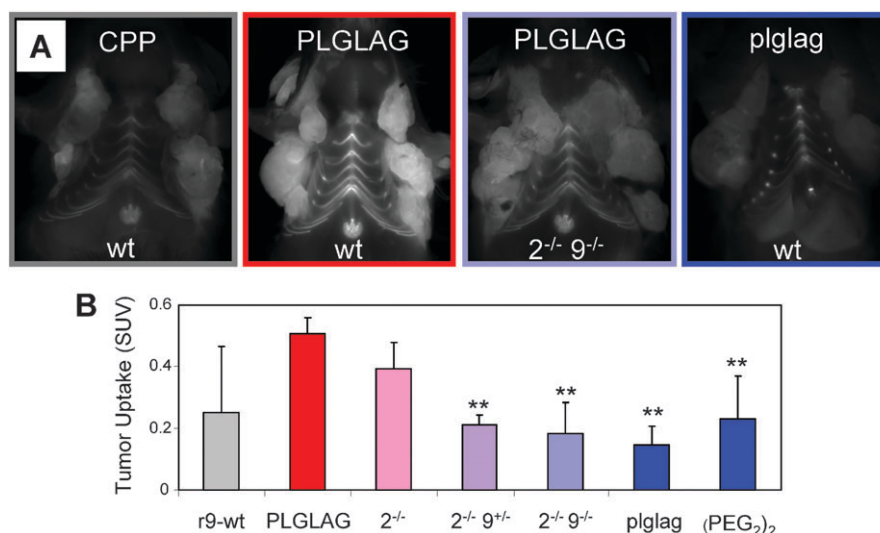

Fig. 2 Uptake of MMP cleavable ACPP's is significantly reduced in PyMT mice lacking the genes for MMP-2 and MMP-9. (A) Images of PyMT animals of the indicated genotype six hours after intravenous injection of the CPP r_9-c(Cy5), the cleavable ACPP (Suc-e$_8$-xPLGLAG-r_9-c(Cy5)), or the D-amino acid negative control (Suc-e$_8$-xplglag-r_9-k(Cy5)) with the skin removed. (B) A chart showing tumor SUVs taken six hours after injection with peptide showing a significant reduction of ACPP uptake in tumors from animals lacking the genes for MMP-2 and MMP-9. r_9-c(Cy5) $n = 3$, PLGLAG $n = 5$, MMP-2$^{-/-}$ $n = 3$, MMP-2$^{-/-}$9$^{+/-}$ $n = 3$, MMP-2$^{-/-}$9$^{-/-}$ $n = 3$, plglag $n = 5$, (PEG2)$_2$ $n = 3$. Error bars represent standard deviations. ** denotes $p < 0.05$ when compared to cleavable PLGLAG ACPP peptide uptake.

an established pattern of MMP-2 and -9 mRNA upregulation in tumor stroma,[24] theoretically generating a convenient model for testing the spatial resolution of ACPPs *in vivo*. To examine whether the pattern of mRNA upregulation correlates to a similar pattern of MMP expression and activation that can be visualized in a whole animal, tumors from PyMT mice were frozen and cryosections were imaged before being stained with DQ gelatin *in situ* zymography.[25] Serial slices were stained with hematoxylin/eosin (H/E), demonstrating nicely that the mRNA upregulation in stroma correlates to MMP activity capable of cleaving ACPPs, which are then taken up in the region of interest (Fig. 3A and ESI, Fig. S7†).
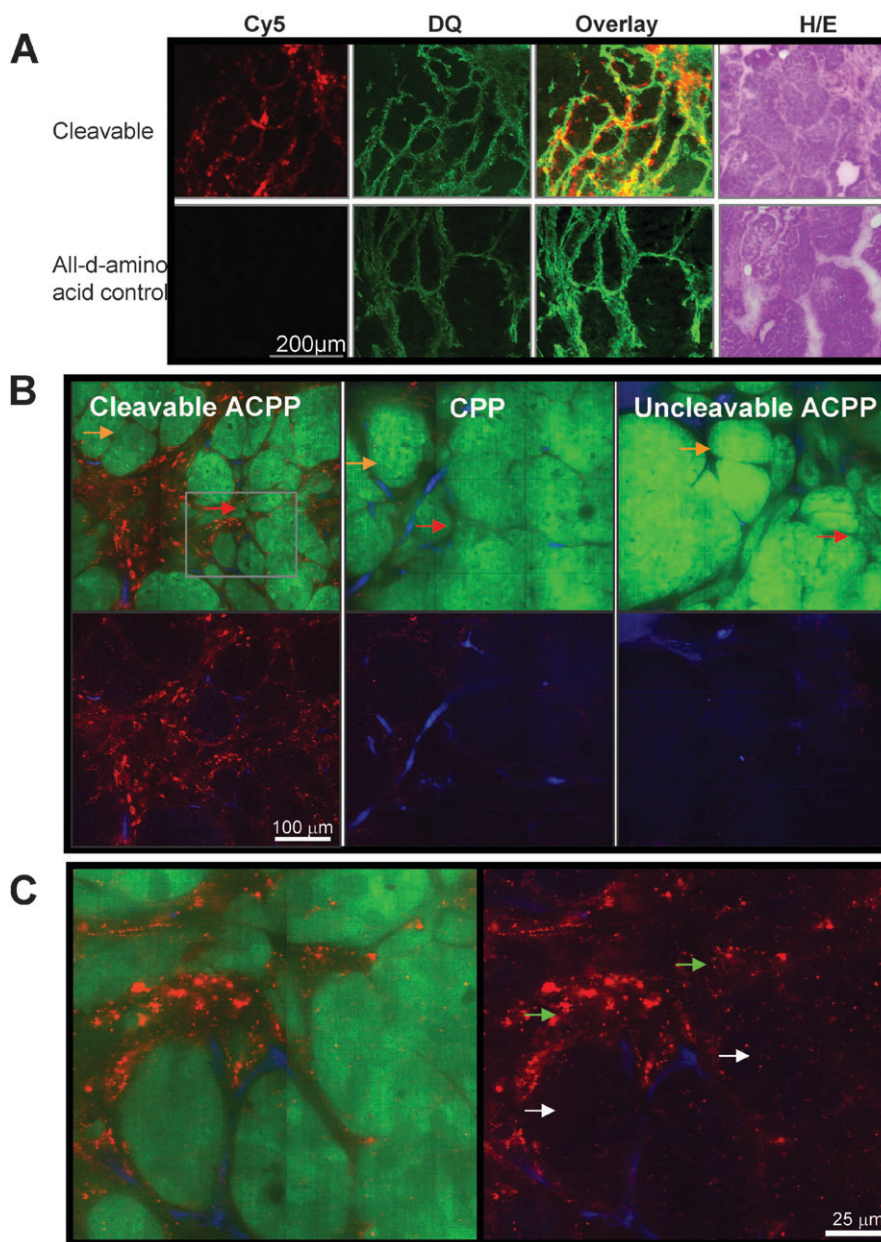

Fig. 3 **Uptake of MMP cleavable ACPP's follows the distribution of MMP's in adenomatous tumors and once cleaved, are delivered to the endosomes of stroma and to a lesser extent tumor cells**. (A) Compares the spatial distribution of fluorescence for cleavable (Suc-e_8-xPLGLAG-r_9-c(Cy5)) or control (Suc-e_8-$x$plglag-r_9-k(Cy5)) peptide in frozen tissue slices six hours after injection of peptide to that of DQ gelatin done on the same slices *post mortem*. H/E stains are shown for adjacent tissue slices for identification purposes. (B) Shows confocal images of tissue from PyMT$^+$ GFP$^{+/+}$ animals six hours after IV injection with cleavable (Suc-e_8-xPLGLAG-r_9-c(Cy5)), cleavage resistant D-amino acid control or CPP (r_9-c(Cy5) control peptide. Cy5 fluorescence is shown in red. Tissues were harvested and imaged five minutes post injection with rhodamine-dextran which labels tumor vasculature shown in blue, demonstrating ACPP accumulation outside of the vascular space in stroma and tumor cells. GFP-expressing tumor epithelial cells are shown in green as overlay or are absent to better visualize peptide and vascular distribution (below). Orange arrows point to areas of more obvious DCIS and red arrows point to areas of likely early invasion. (C) Enlarged window of cleavable ACPP demonstrated more clearly that the uptake into the stroma (green arrows) and tumor cell (white arrows) is reminiscent of endosomal puncta.

In vivo confocal microscopy on living tissue demonstrates that uptake in tumor stroma is extravascular and localized to endosomes.

In order to better evaluate the spatial distribution in the microenvironment, PyMT GFP$^{+/+}$ animals were injected with r$_9$-c(Cy5) CPP, cleavable ACPP, and D-amino acid ACPP peptide. At six hours, the mice were intravenously injected with 5 mDa rhodamine dextran to label the blood vessels. Following gross imaging *in situ*, the tumors were immediately excised and imaged by confocal microscopy to determine the macro and subcellular distribution in live tissue, as done in Aguilera *et al.* in 2009.[21] Consistent with the SUV values shown in Fig. 2, the resultant images clearly show a greater uptake of cleavable peptide than both the CPP and D-amino acid ACPP in all locations. The most significant area of uptake was at the tumor–stroma boundary in areas of ductal carcinoma *in situ* (DCIS) and likely early invasion (Fig. 3B, orange and red arrows, respectively). Additionally, it was observed that the peptide penetrated well beyond the blood vessels, even deep into DCIS nodules, though to a much lesser

extent than stroma (Fig. 3C, white arrows). In all cases, the peptide appeared to be in punctae, probably in subcellular compartments or in the extracellular matrix, as seen previously in xenografts (Fig. 3C). Though we are unable to provide an exact figure for spatial resolution for either the ACPPs or the DQ, taken together, these data suggest that ACPPs are likely to remain in close proximity to the site of cleavage after enzymes have acted upon them, probably due to the strong electrostatic interactions of polyarginines with the extracellular matrix components and subsequent endocytosis.

Detection of lung metastasis in PyMT mouse model with ACPPs

A second strategy for looking at spatial resolution in an animal model is that of metastasis. Many targeting schemes are able to reach primary tumors, but metastases are a more difficult problem due to their small size, and relative lack of enhanced permeability and retention to retain probe at the site of activation. The PyMT model is known to metastasize to the lung, so lungs were dissected out to determine if metastases
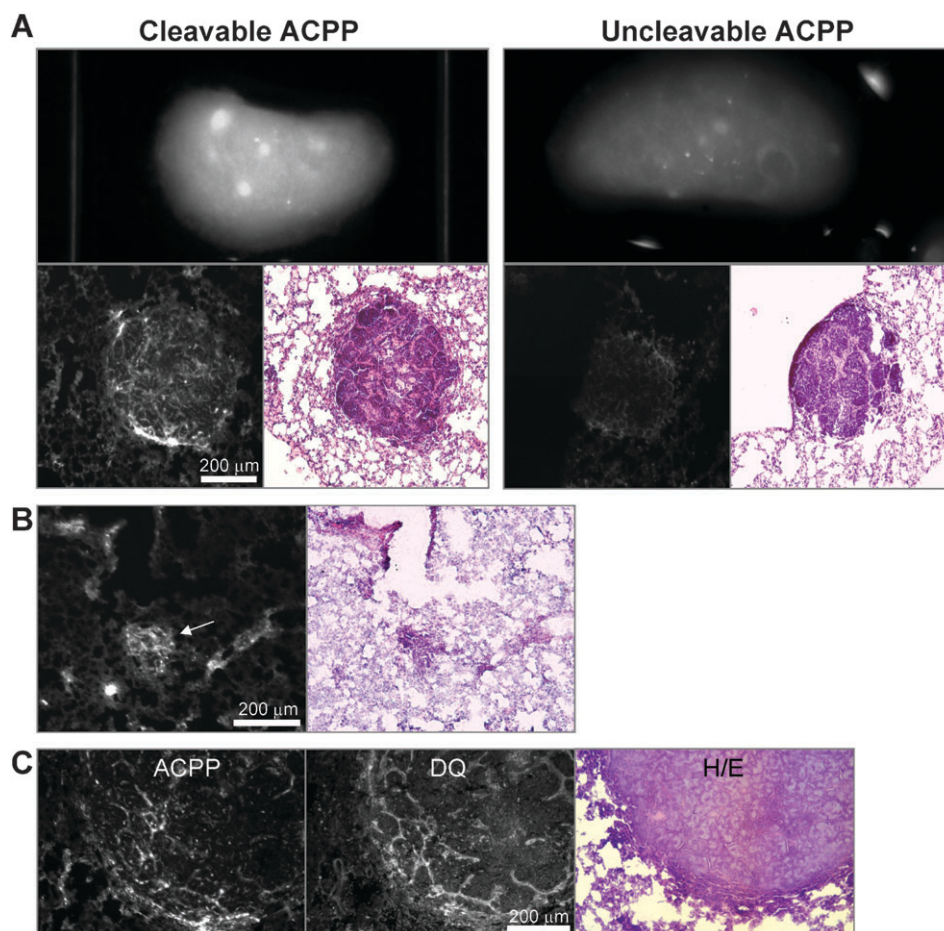

Fig. 4 **ACPPs accumulate in spontaneous lung metastases in PyMT mice**. (A) Gross images of dissected lung lobes from animals six hours after injection with either the cleavable (Suc-e$_8$-xPLGLAG-r$_9$-c(Cy5)) or cleavage resistant control (Suc-e$_8$-$x$plglag-r$_9$-k(Cy5)). Lungs were then frozen, sectioned, imaged by fluorescence histology to visualize the microdistribution of the peptide (lower left), and serial sections were stained with H/E (lower right) to demonstrate the presence of metastases. (B) Contrast of metastases as small as 100 µm (white arrow) were detected in tissue sections. (C) DQ gelatin *in situ* zymography was performed on the same frozen section of cleavable ACPP (imaged by Cy5 fluorescence) metastasis showing substantial colocalization of peptide uptake to enzyme activity in the metastases.

were present and if there was accumulation of fluorescence at the site of metastasis. As expected, approximately 10% of the 12–14 week old animals examined had metastases that were consistently brighter than lung parenchyma. Furthermore, these metastases were much brighter in lungs from animals injected with cleavable peptide than in those injected with the D-amino acid control peptide (Fig. 4A). To examine the histological distribution, lung lobes were sectioned and fluorescence images were taken prior to staining with H/E. This revealed significant contrast at the histological level for the cleavable peptide which was much greater than uncleavable peptide (Fig. 4A). A significant contrast between metastasis and adjacent lung parenchyma was additionally detectable in metastases as small as 0.1 mm (Fig. 4B, white arrow). To verify that uptake in metastases was due to enzyme activity, histological sections were imaged by fluorescence to determine localization of Cy5 peptide and subsequently analyzed by DQ *in situ* zymography. The same section analyzed for peptide fluorescence and *in situ* zymography showed that enzyme activity and peptide distribution was localized predominantly to the invasive edge and stroma of the metastases, which was very similar to what was previously observed in primary tumors (Fig. 4C). Serial sections were H/E stained to verify the identity of the metastases.

Macromolecular carriers enhance tumor uptake, decrease rate of excretion, and eliminate significant joint and cartilage uptake

As is clear from the images and SUVs, both cleavable and control ACPPs accumulate more strongly in the cartilage, liver and kidney than in tumors (Fig. 5A–D). Some of the uptake into cartilage, especially in the joints, is independent of protease cleavage because it occurs even with the negative controls (Fig. 1A, 2A, 5B). We suspect that the extremely high concentration of proteoglycans in cartilage begins to compete with the intramolecular polyglutamate domain in binding to the polyarginine domain (ESI, Fig. S8†). Another component of the cartilage uptake does depend on MMP-2 and -9, because transgenic deletion of both MMP-2 and -9 reduces uptake, for example in ventral ribs (Fig. 2A).

Due to the high kidney uptake and urinary excretion of uncleaved peptide, we hypothesized that tumor uptake could be increased both in absolute terms and relative to normal tissues if the ACPPs were attached to a macromolecule large enough to prevent rapid excretion *via* renal filtration, but small enough to permit diffusion into solid tumors. The increased circulation time due to increased blood half-life should give more time for tumor MMPs to cleave a larger fraction of the injected material. To this end, we appended the macromolecule to the polyglutamate domain so that both would be jettisoned by linker cleavage, leaving the polyarginine and cargo unperturbed. The 12 kDa poly(ethyleneglycol) used in our initial study was not large enough to prevent glomerular filtration.[12] Next, we tried several ~70 kD macromolecules, including a fifth-generation poly(amidoamine) dendrimer (Fig. 6B), mouse serum albumin (Fig. 6D) and a 70 kD dextran with approximately nine negative charges (Fig. 6E). All three carriers increased the blood half-life in circulation and peak SUVs in tumors as anticipated, though peak contrast
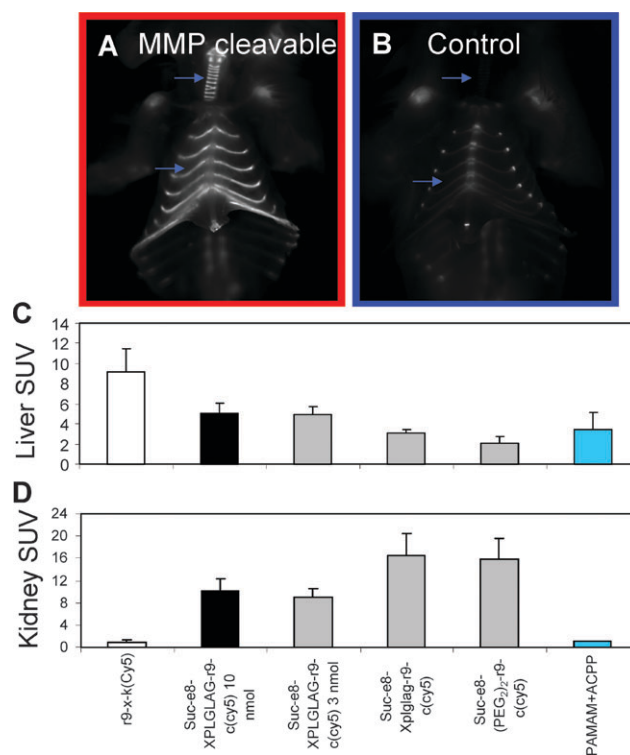

Fig. 5 Free ACPPs accumulate in the cartilage, liver and kidney, as well as the tumor. (A) and (B) show animals six hours after injection with either the cleavable (Suc-e$_8$-xPLGLAG-r$_9$-c(Cy5)) (A) or control (Suc-e$_8$-xplglag-r$_9$-k(Cy5)) (B) peptides. Skin and pectoralis muscle have been removed, exposing the ribs and thoracic cage. Significant uptake is localized to cartilage, which is specific to cleavable peptide (blue arrows). (C) and (D) show standardized uptake values for the liver (C) and kidney (D) for animals injected with the r$_9$-x-k(Cy5) cleavable peptide at 10 and 3 nmol doses, the D-amino acid control, the (PEG2)$_2$ control, and a PAMAM conjugated ACPP. These data show there is high uptake in the liver and kidney with free ACPP peptides and that kidney uptake decreases significantly as a result of adding macromolecular weight carriers. r$_9$-x-k(Cy5) $n = 3$, xPLGLAG 10 nmol $n = 9$, xPLGLAG 3 nmol $n = 3$, (PEG2)$_2$ $n = 3$, PAMAM + ACPP $n = 2$. The error bars are standard deviations.

was delayed until 24–48 h after injection, rather than 6 h (Fig. 6C). Attachment to albumin or dextran increased the tumor SUVs of both cleavable ACPPs and uncleavable controls, so that their ratio remained about 4 or 5 (Fig. 6D–F). The increase in SUV for the uncleavable conjugates may be due to the enhanced permeability and retention (EPR) effect of leaky tumor vasculature.[26] Although we found that the cleavage rate was slower once molecules had been attached to a large molecular weight carrier, we found that adding the carrier did not appreciably affect the histological distribution of the ACPP (ESI, Fig. S10†).

Attachment of ACPPs to macromolecular carriers confers an additional bonus, the near-complete elimination of uptake by cartilage (Fig. 6B) as well as kidneys (Fig. 5D). The addition of just a 5 kDa PEG to the polyglutamate end of the ACPP is sufficient to significantly reduce joint and synovial uptake (data not shown), suggesting that uptake occurs subsequent to synovial filtration.[27] Reducing renal uptake requires a larger carrier, suggesting that the decrease is
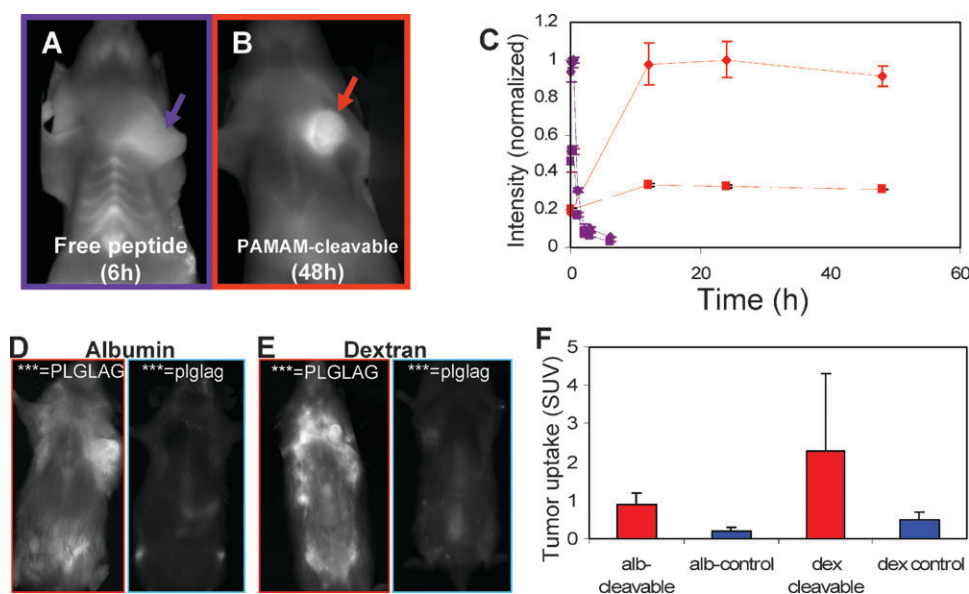
Fig. 6 **Addition of a large molecular carrier to the polyglutamate results in greater uptake in tumor**. (A) and (B) show fluorescent images of live mice 6 and 48 h (time of maximal contrast) after injection with cleavable peptide (Suc-e_8-xPLGLAG-r_9-c(Cy5)) (A) and cleavable peptide attached to a generation 5 PAMAM dendrimer (PAMAM-e_9-xPLGLAG-r_9-k(Cy5)) (B), respectively. (C) A time course of fluorescence contrast showing the difference in washout from the tumor and tissues for the two constructs. Solid lines represent the tumor and dashed lines the thoracic background for the free peptide (purple) and carrier attached construct (red). Data is representative of $n = 2$ mice each and the error bars are standard deviations. (D) and (E) show animals 48 h after injection with cleavable and cleavage resistant peptides attached covalently to albumin (D) and dextran (E), respectively (albumin or dextran-e_9-xPLGLAG-r_9-k(Cy5)). (F) shows SUV of tumors for the cleavable and D-amino acid cleavage resistant constructs shown in (D) and (E) ($n = 2$ each).

accomplished by a reduction in glomerular filtration. One might expect that liver uptake would be increased by the addition of a large molecular weight carrier, which shifts the excretion pathway away from the kidneys towards the hepatobiliary and reticulendothelial systems. Fortunately, at least for the dendrimeric carriers liver SUVs are not significantly changed (Fig. 5C), so the macromolecular carriers improve the ratios of tumor SUVs to those of all other tissues.

Discussion

We have provided evidence that ACPPs represent a general strategy for high resolution, enzyme-specific, *in vivo* imaging of tumors. ACPPs perform well, not only in traditional xenograft models in immunocompromised mice (Fig. 1), but also in transgenic tumors (Fig. 2A) and metastases (Fig. 4) in syngeneic animals. Genetic deletion of MMP-2 and -9 together (Fig. 2B) or administration of MMP inhibitors (Fig. 1C) reduced tumor uptake down to the level observed with uncleavable control peptides. Higher magnification images showed that uptake was highest at the tumor–stromal boundary (Fig. 3 and 4), corresponding to the previously reported distribution of MMP activity as well as independent *in situ* zymography done on adjacent frozen slices. These data suggest that ACPPs not only penetrate beyond blood vessels, but can penetrate deep into tumor nodules, thereby potentially increasing their utility as *in vivo* protease sensors. The background in the kidney and joints, while high in minimal-sized peptides (Fig. 5), could be decreased dramatically by the addition of a macromolecular carrier to

the polyglutamate side of the molecule. The decrease in background as well as increase in tumor uptake combined to provide an improved contrast with the larger molecular weight probes. (Fig. 6).

Although xenografts of human tumors into immuno-compromised mice are traditional tumor models, transgenic mouse models such as the PyMT model enable an examination of the spontaneous development of a tumor in a syngeneic microenvironment. Since the host has a competent immune system, important inflammation-associated factors in the tumor microenvironment can better mimic those found in human patients. Moreover, the PyMT tumors spontaneously metastasize from the mammary gland to the lung, just as many human breast cancers do. It is therefore important that ACPPs give good contrast for transgenic tumors (both primary and metastatic), as well as for xenografts. Furthermore, a transgenic model permits genetic ablation of MMP-2 and -9, which is currently the most rigorous test for the role of these two enzymes in generating contrast. Even though the linker sequence used here, PLGLAG, is only moderately selective for MMP-2 and -9 *in vitro* (Aguilera *et al.*, accompanying paper[21]), the *in vivo* data from the double knockout indicates that these enzymes are indeed jointly responsible for the protease-dependent component of tumor uptake. By contrast, the ability of MMP inhibitors to reduce uptake into xenografts was not quite as complete, though SB3-CT, an inhibitor relatively specific for MMP-2 and -9,[16] was as effective as prinomastat, a broader-spectrum MMP inhibitor. Most previous attempts to image MMP activities *in vivo* either failed to test MMP ablation/inhibition or relied on just one broad-spectrum inhibitor.[9,10,12,28,29]

ACPPs can show fairly sharp boundaries between regions of high and low uptake (Fig. 5D of Aguilera et al., accompanying paper;[21] Fig. 3 and 4 of current paper). Regions of high ACPP uptake correspond closely to regions of high MMP activity as visualized by in situ zymography (Fig. 3A), which has the highest spatial resolution of all established methods for assessing MMP activity. The colocalization between products of ACPP cleavage in vivo and products of DQ gelatin cleavage post mortem suggests that MMP-2/9 activity is genuinely quite tightly localized, and that the majority of polyarginine motifs released from ACPPs are rapidly immobilized before they can diffuse more than a few tens of microns. This spatial resolution enables ACPPs to highlight metastases as small as ~100 μm (Fig. 4B), a size range that would be highly desirable for early detection. Unfortunately, the severity of light scattering means that optical imaging can preserve such lateral resolution only quite close to the surface of exposed tissues, as in surgery or endoscopy. Other modalities such as magnetic resonance imaging (MRI) are better suited to whole-body scanning at high spatial resolution. Unlike probes that can only work by optical dequenching,[8–10,30,31] ACPPs are generalizable to magnetic contrast agents, as we will report separately.

Attachment of macromolecular carriers such as albumin, dextran or PAMAM dendrimers to ACPPs drastically reduces uptake by the kidney and joints, probably because the macromolecules (final MW ~ 70 kDa) are too large to pass through pores in the glomeruli and cartilage. Meanwhile accumulation in tumors is enhanced by up to 5 fold, probably for two reasons. First, the longer circulating lifetime of macromolecules compared to peptides gives the former more time to be cleaved by the MMPs in and around the tumor. Second, the "enhanced permeability and retention" (EPR) effect tends to concentrate macromolecules in tumors whose vasculature is leakier than that of normal tissue, but EPR does not affect small peptides. EPR cannot be the primary mechanism for accumulation, because conjugates of cleavable ACPPs still give much higher uptake than identically-sized conjugates of their D-amino acid controls, but EPR could still help increase enzyme and substrate coincidence of MMPs to cleave the ACPP linker. We prefer not to increase the size of the macromolecular conjugate much beyond 70 kDa, because penetration into the core of solid tumors becomes too inefficient and excretion of uncleaved probe becomes too slow. Of the three macromolecular carriers tested, albumin and dextran have the longest history of pharmaceutical acceptability, but PAMAM dendrimers have given the most reproducible behavior in our hands. Carrier-less peptides do have two remaining advantages, ease of synthesis, and relatively fast pharmacokinetics and appearance of contrast. Fast kinetics would be important if the imaging must be done as soon as possible after injection, for example in nuclear imaging with short-lived isotopes.

We believe that optical probes should not be evaluated merely by the optical contrast they give between tumor and background, which is strongly affected by tissue depth and pigmentation, and can be biased by the choice of local region and signal thresholding. Quantitative accumulations of fluorophore should also be measured after dissection and homogenization. Such uptakes can be expressed as %ID g^{-1} or SUV; we prefer the latter because it normalizes for body weight and becomes dimensionless. In a previous paper,[12] we discussed grinding up tissues and comparing their fluorescence emission using liver as a standard, but further investigation showed that the same amount of Cy5-labeled peptide gave significantly different fluorescence intensities in different tissues, so each tissue needs its own calibration curve. Once this is done, we feel that carefully done fluorescence-based SUVs can be as reliable as SUVs based on liquid scintillation counting of radioisotope, which are also subject to tissue-specific quenching. One technical problem observed during the course of these experiments was that there is no single perfect negative control. In theory, the D-amino acid control probe should be better than the control probe with the (PEG2)$_2$ linker, since it retains the chemical properties of the amino acids but should not be cleaved by most biological enzymes. However, we found SUV's for the probe with the (PEG2)$_2$ linker to be lower than the D-amino acid control in HT-1080 tumors and liver. This was explained by gel electrophoresis of the small amount of labeled peptide retained in these tissues (Fig. 1D and ESI, Fig. S9†), which showed that the D-amino acid control had undergone cleavage, whereas the probe with the (PEG2)$_2$ linker had not. Cleavage of the D-amino acid control is probably due to enzymes that can cut next to Gly, which has no chirality. In PyMT tumors (Fig. 2) and kidney (Fig. 5D), SUVs were similar between the two control linkers, which is consistent with the lack of cleavage of either peptide in these tissues (ESI, Fig. S9†).

ACPPs improve on CPPs by providing a targeting mechanism, e.g. to tumors, and reducing systemic toxicity (discussed in Aguilera et al., 2009).[21] The current study has verified the enzymatic specificity, spatial resolution, and tumor generality beyond the initial report of Jiang et al.,[12] and has shown that tumor specificity over background tissues can be significantly improved by adding appropriate macromolecular carriers. Future reports will focus on designing alternate substrate sequences, broadening the range of payloads to include nanoparticles, contrast agents for magnetic resonance imaging and chemotherapeutics, and expanding the use of ACPPs to other common protease-dependent pathologies such as atherosclerosis and strokes.

Experimental

Peptides

Cleavable ACPP Suc-e$_8$-xPLGLAG-r$_9$-c(Cy5)-NH$_2$, D-amino acid cleavage-resistant control Suc-e$_8$-xplglag-r$_9$-k(Cy5)-NH$_2$, uncleavable control Suc-e$_8$-(PEG2)$_2$-r$_9$-c(Cy5)-NH$_2$, CPP r$_9$-c(Cy5)-NH$_2$, and CPP r$_9$-x-k(Cy5) were synthesized and labeled with Cy5 (GE Healthcare), where x = 6-amino-hexanoic acid. Briefly, peptides were synthesized on an automatic peptide synthesizer (Perceptive Biosystems Pioneer or PTI Prelude) following standard procedures for fluorenyl-methoxycarbonyl solid-phase synthesis. Peptides were N-terminally capped with a succinyl (Suc) group to provide

a ninth negative charge equivalent to glutamate without an amino group, and C-termini were amidated. After cleavage off the resin, the C-termini were either labeled through the cysteine with Cy5 monomaleimide or through the lysine with Cy5 mono-NHS ester. Peptides were purified using HPLC. The molecular weight of all peptides was confirmed by mass spectroscopy, and the concentration of each peptide stock solution was verified by UV-Vis absorbance. The conjugation of macromolecules to ACPPs is described in the ESI.†

Animals

Nude mice harboring HT-1080 tumors (3–8 mm) were obtained from Explora Biosciences (San Diego, CA). Transgenic mice carrying the polyoma middle T oncogene driver by the MMTV promoter in the FVB background (PyMT mice) and associated PyMT:MMP KO transgenic mice were bred and housed at UCSD. MMP-2 and -9 knockout mice were generously provided by the Coussens laboratory (UCSF), and β-actin::GFP FVB mice were purchased from Jackson labs. Genotypes were verified by PCR analysis. Nude mice bearing PC3, HCCT and Hep2 were obtained from Dr Robert Hoffman at Anticancer, Inc (San Diego, CA). All other xenografts were produced in the lab by injecting $1–5 \times 10^6$ cells into the mammary fat pad of either athymic nude mice (HT-1080s) or albino C57BL/6 mice (Jackson Labs) (F16/F10 melanoma, 8119, and 230 cells). Prinomastat (Pfizer) was injected IP at a dose of 4.5 mg every 12 h for 24 h prior to the experiment for a total of 13.5 mg/mouse. 500 μg SB3CT (MMP2/9 inhibitor 5, EMD) was injected IP in 50 μL DMSO 2 h prior to the experiment. All animal procedures were approved by UCSD's institutional animal care and use committee.

Optical imaging

Animals were anesthetized with 80 mg kg^{-1} ketamine and 40 mg kg^{-1} midazolam. 1–10 nmols of each probe was injected intravenously. Animals were imaged at 1 s and at 3 s using a Maestro spectral deconvolution imager (CRI, Boston, MA) with excitation using 640/48 nm band pass filter and emission filter tuned to 700 nm after passing light through a 700 LP filter (resulting bandwidth was 700–720 nm). Animals were imaged during the first hour after injection and then allowed to wake up. At 6 h, and when applicable, 24 h and 48 h, animals were re-anesthetized and imaged. At given time points, animals were sacrificed, organs harvested and imaged (such as thorax as in Fig. 5A), at the same settings as above and tissues were frozen. For lung metastases, lungs were inflated with 50 : 50 PBS–cryoprotectant (OCT Compound, Tissue-Tek) prior to imaging then freezing. For experiments using albumin and dextran conjugated peptides, imaging was done exciting with 620/20 filter and tuning the emission to 680 nm.

Standardized uptake values

Frozen tissues were thawed and cut into 30 mg samples. For heterogeneous tumors such as the PyMT tumors, two to three 30 mg samples were processed separately and averaged. Each 30 mg of tissue was then homogenized with 100 μL SDS lysis buffer (1% SDS, 20 mM Tris buffer, pH 7.6) using a pestle and then heated to 80 °C for 10 min. Tissues were microwaved twice for 4 s, centrifuged for 10 min, frozen, and imaged using the Maestro. Integrated intensities were calculated using Image J (free peptides) or averages taken with Adobe Photoshop (albumin and dextran conjugates only). Standards were prepared the same with tumor, liver, kidney and muscle from uninjected animals, spiking them with known amounts of the r9-x-k(Cy5) peptide. Calibration intensities were fit to a linear curve and the slope was used as a calibration factor (ESI, Fig. S2). From these standard curves, standardized uptake values (SUV) were determined, defined as (moles g^{-1} tissue)/(moles injected/weight of the animal), and were normalized to a calibration standard (USFS-336 Orange, Labsphere Inc.) to correct for changes in light levels over time. Since limited tissue was available for most xenografted tumor types, PyMT tumors were used as the calibration tissue for calculating standardized uptake values, instead of calibrating to each xenografted tumor type individually. Percent inhibition was calculated as (SUVcleavable − SUVinhibitor)/(SUVcleavable − SUVuncleavable).

Peptide gels

SUV lysates were diluted 1 : 3 in 33% PBS–66% sample buffer, electrophoresed on tricine buffered 10–20% polyacrylamide gels (Invitrogen) according to the manufacturer's instructions and imaged for Cy5 fluorescence in the Maestro small animal imager.

Fluorescence histology

Frozen sections were cut at 20 μm thickness for HT-1080 and PyMT tumors and 25 μm for PyMT metastases then examined using a fluorescence dissecting microscope (Lumar, Zeiss) (exposure times 5–15 s, ex 620/60, em 700/75). For in situ zymography, DQ gelatin (Invitrogen) was processed following the manufacturer's instructions and imaged with a fluorescence dissection microscope (exposure times 1–5 s, ex 470/40, em 525/50). Serial sections were stained using a standard hematoxylin and eosin procedure, and imaged using a light microscope (Axiovert, Zeiss).

Confocal imaging of PyMT tumors

For confocal imaging, β-actin::GFP$^{+/+}$ FVB mice (Jackson Labs) were bred with PyMT mice to generate PyMT GFP$^{+/+}$ mice. Mice were injected intravenously with 1 mg of 2 MDa Rhodamine Dextran in 50 μL 5 min before sacrifice to visualize the blood pool by microscopy. After sacrifice, tumors were excised, kept on ice in HBSS until imaged, placed on a cover slip and imaged by confocal microscopy (LSM 5 Live, Zeiss). Tissues were imaged within 30 min of sacrifice, imaged with an automatic stage in tile mode (5 × 5 images for total of 25 fields of view) at one z-position. These large images were taken at 400×, yielding 5000 pixel × 5000 pixel images with a total area of approximately 795 μm × 795 μm. This method enabled both high resolution images at the subcellular level as well as a broader view of the tumor and microenvironment. Cy5 peptide, GFP tumor cells and rhodamine were excited

with 635 nm, 488 nm and 532 nm lasers, with emission acquired with 650 nm LP, 505 nm LP and 550 nm LP filters, respectively.

Abbreviations

CPP   cell penetrating peptide
ACPP   activatable cell penetrating peptide
MMP-   matrix metalloproteinase
SUV   standardized uptake value
EPR   enhanced permeability and retention
PyMT   polyoma middle T oncogene driven by mouse mammary tumor virus promoter spontaneous model of cancer

References

1 V. Chabottaux and A. Noel, Breast cancer progression: insights into multifaceted matrix metalloproteinases, *Clin. Exp. Metastasis*, 2007, **24**, 647–656.
2 T. Turpeenniemi-Hujanen, Gelatinases (MMP-2 and -9) and their natural inhibitors as prognostic indicators in solid cancers, *Biochimie*, 2005, **87**, 287–297.
3 A. Z. Gimeno-García, A. Santana-Rodríguez, A. Jiménez, A. Parra-Blanco, D. Nicolás-Pérez, C. Paz-Cabrera, F. Díaz-González, C. Medina, L. Díaz-Flores and E. Quintero, Up-regulation of gelatinases in the colorectal adenoma-carcinoma sequence, *Eur. J. Cancer*, 2006, **42**, 3246–3252.
4 D. Trudel, Y. Fradet, F. Meyer, F. Harel and B. Tetu, Significance of MMP-2 Expression in Prostate Cancer: an Immunohistochemical Study, *Cancer Res.*, 2003, **63**, 8511–8515.
5 T. Leinonen, R. Pirinen, J. Böhm, R. Johansson, K. Ropponen and V.-M. Kosma, Expression of matrix metalloproteinases 7 and 9 in non-small cell lung cancer. Relation to clinicopathological factors, beta-catenin and prognosis, *Lung Cancer*, 2006, **51**, 313–321.
6 R. Oltenfreiter, L. Staelens, V. Kersemans, B. Cornelissen, F. Frankenne, J.-M. Foidart, C. Van de Wiele and G. Slegers, Valine-based biphenylsulfonamide matrix metalloproteinase inhibitors as tumor imaging agents, *Appl. Radiat. Isot.*, 2006, **64**, 677–685.
7 J. F. Fisher and S. Mobashery, Recent advances in MMP inhibitor design, *Cancer Metastasis Rev.*, 2006, **25**, 115–136.
8 C. Bremer, S. Bredow, U. Mahmood, R. Weissleder and C. H. Tung, Optical imaging of matrix metalloproteinase-2 activity in tumors: feasibility study in a mouse model, *Radiology*, 2001, **221**, 523–529.
9 C. Bremer, C. H. Tung and R. Weissleder, In vivo molecular target assessment of matrix metalloproteinase inhibition, *Nature Med.*, 2001, **7**, 743–748.
10 J. O. McIntyre, B. Fingleton, K. S. Wells, D. W. Piston, C. C. Lynch, S. Gautam and L. M. Matrisian, Development of a novel fluorogenic proteolytic beacon for in vivo detection and imaging of tumour-associated matrix metalloproteinase-7 activity, *Biochem. J.*, 2004, **377**, 617–628.
11 M. Lepage, W. C. Dow, M. Melchior, Y. You, B. Fingleton, C. C. Quarles, C. Pépin, J. C. Gore, L. M. Matrisian and J. O. McIntyre, Noninvasive detection of matrix metalloproteinase activity in vivo using a novel magnetic resonance imaging contrast agent with a solubility switch, *Mol. Imaging*, 2007, **6**, 393–403.
12 T. Jiang, E. S. Olson, Q. T. Nguyen, M. Roy, P. A. Jennings and R. Y. Tsien, Tumor imaging by means of proteolytic activation of cell-penetrating peptides, *Proc. Natl. Acad. Sci. U. S. A.*, 2004, **101**, 17867–17872.
13 E. A. Goun, R. Shinde, K. W. Dehnert, A. Adams-Bond, P. A. Wender, C. H. Contag and B. L. Franc, Intracellular Cargo Delivery by an Octaarginine Transporter Adapted to Target Prostate Cancer Cells through Cell Surface Protease Activation, *Bioconjugate Chem.*, 2006, **17**, 787–796.
14 Y. Zhang, M. K. So and J. Rao, Protease-modulated cellular uptake of quantum dots, *Nano Lett.*, 2006, **6**, 1988–1992.
15 D. R. Shalinsky, J. Brekken, H. Zou, S. Kolis, A. Wood, S. Webber and K. Appelt, Antitumor efficacy of AG3340 associated with maintenance of minimum effective plasma concentrations and not total daily dose, exposure or peak plasma concentrations, *Invest. New Drugs*, 1998, **16**, 303–313.
16 O. Kleifeld, L. P. Kotra, D. C. Gervasi, S. Brown, M. M. Bernardo, R. Fridman, S. Mobashery and I. Sagi, X-ray absorption studies of human matrix metalloproteinase-2 (MMP-2) bound to a highly selective mechanism-based inhibitor. Comparison with the latent and active forms of the enzyme, *J. Biol. Chem.*, 2001, **276**, 17125–17131.
17 M. Maatta, Y. Soini, A. Liakka and H. Autio-Harmainen, Differential Expression of Matrix Metalloproteinase (MMP)-2, MMP-9, and Membrane Type 1-MMP in Hepatocellular and Pancreatic Adenocarcinoma: Implications for Tumor Progression and Clinical Prognosis, *Clin. Cancer Res.*, 2000, **6**, 2726–2734.
18 D. Jinga, M. Stefanescu, A. Blidaru, I. Condrea, G. Pistol and C. Matache, Serum levels of matrix metalloproteinases MMP-2 and MMP-9 and their tissue natural inhibitors in breast tumors, *Roum. Arch. Microbiol. Immunol.*, 2004, **63**, 141–158.
19 M. Lacroix, Persistent use of "false" cell lines, *Int. J. Cancer*, 2008, **122**, 1–4.
20 C. T. Guy, R. D. Cardiff and W. J. Muller, Induction of mammary tumors by expression of polyomavirus middle T oncogene: a transgenic mouse model for metastatic disease, *Mol. Cell. Biol.*, 1992, **12**, 954–961.
21 T. A. Aguilera, E. S. Olson, M. M. Timmers, T. Jiang and R. Y. Tsien, Systemic in vivo distribution of activatable cell penetrating peptides is superior to that of cell penetrating peptides, *Integr. Biol.*, 2009, **1**, DOI: 10.1039/b904890a.
22 A. Ducharme, S. Frantz, M. Aikawa, E. Rabkin, M. Lindsey, L. E. Rohde, F. J. Schoen, R. A. Kelly, Z. Werb, P. Libby and R. T. Lee, Targeted deletion of matrix metalloproteinase-9 attenuates left ventricular enlargement and collagen accumulation after experimental myocardial infarction, *J. Clin. Invest.*, 2000, **106**, 55–62.
23 E. Y. Lin, J. G. Jones, P. Li, L. Zhu, K. D. Whitney, W. J. Muller and J. W. Pollard, Progression to malignancy in the polyoma middle T oncoprotein mouse breast cancer model provides a reliable model for human diseases, *Am. J. Pathol.*, 2003, **163**, 2113–2126.
24 T. X. Pedersen, C. J. Pennington, K. Almholt, I. J. Christensen, B. S. Nielsen, D. R. Edwards, J. Rømer, K. Danø and M. Johnsen, Extracellular protease mRNAs are predominantly expressed in the stromal areas of microdissected mouse breast carcinomas, *Carcinogenesis*, 2005, **26**, 1233–1240.
25 W. M. Frederiks and O. R. Mook, Metabolic mapping of proteinase activity with emphasis on in situ zymography of gelatinases: review and protocols, *J. Histochem. Cytochem.*, 2004, **52**, 711–722.
26 Y. Matsumura and H. Maeda, A new concept for macromolecular therapeutics in cancer chemotherapy: mechanism of tumoritropic accumulation of proteins and the antitumor agent smancs, *Cancer Res.*, 1986, **46**, 6387–6392.
27 A. Maroudas, Transport of solutes through cartilage: permeability to large molecules, *J. Anat.*, 1976, **122**, 335–347.

28 T. J. Harris, G. von Maltzahn, M. E. Lord, J.-H. Park, A. Agrawal, D.-H. Min, M. J. Sailor and S. N. Bhatia, Protease-triggered unveiling of bioactive nanoparticles, *Small*, 2008, **4**, 1307–1312.

29 R. Lebel, B. Jastrzębska, H. Therriault, M.-M. Cournoyer, J. O. McIntyre, E. Escher, W. Neugebauer, B. Paquette and M. Lepage, Novel solubility-switchable MRI agent allows the noninvasive detection of matrix metalloproteinase-2 activity *in vivo* in a mouse model, *Magn. Reson. Med.*, 2008, **60**, 1056–1065.

30 U. Mahmood, C. H. Tung, A. Bogdanov, Jr and R. Weissleder, Near-infrared optical imaging of protease activity for tumor detection, *Radiology*, 1999, **213**, 866–870.

31 R. Weissleder, C. H. Tung, U. Mahmood and A. Bogdanov, Jr, *In vivo* imaging of tumors with protease-activated near-infrared fluorescent probes, *Nat. Biotechnol.*, 1999, **17**, 375–378.